Sustainable Materials and Technologies 36 (2023) e00603

Contents lists available at ScienceDirect

Sustainable Materials and Technologies

journal homepage: www.elsevier.com/locate/susmat

An order magnitude increase in energy of Li-ion capacitors by adopting combined insertion-conversion process with long durability and water soluble binder

Manohar Akshay [a], Krishnan Subramanyan [a], Yun-Sung Lee [b,*], Vanchiappan Aravindan [a,*]

[a] Department of Chemistry, Indian Institute of Science Education and Research (IISER), Tirupati 517507, India
[b] School of Chemical Engineering, Chonnam National University, Gwang-ju 61186, Republic of Korea

ARTICLE INFO

Keywords:
Li-ion capacitor
Anode
Conversion
Insertion
Li-ion battery recycling

ABSTRACT

Lithium-ion capacitors (LICs) are one of the most promising energy storage devices with both high-energy density and high-power characteristics. Our work reports the demonstration of high energy and high power LIC assembly by introducing the combination of insertion-conversion mechanisms as a battery-type electrode with commercial activated carbon (AC) as the capacitor-type electrode. Accordingly, the conversion type copper oxide (CuO) and insertion host, graphite (RG) are formulated as composite *via* mechanical milling and employed as active material. Both RG and CuO have been recovered/regenerated from the anodic active material, and the Cu-foil current collector of spent Li-ion batteries is worth mentioning. The electrochemical performance of different RG:CuO composites are analyzed using two binders (PVdF, Polyvinylidene fluoride & CMC, Carboxymethylcellulose), and the CMC is found to be dominant in comparison with PVdF in the half-cell assembly. An *in-situ* impedance is performed to understand the interfacial properties. Prior to the fabrication of LIC, the battery-type electrode is electrochemically pre-lithiated (LiC_6 + Cu^0+ Li_2O) and paired with the AC electrode under the balanced mass loading. The LIC with RG(50):CuO(50) anode and AC cathode rendered a maximum energy density of ~198.7 Wh kg^{-1} with superior cyclic stability for 10,000 cycles. Also, the LIC is subjected to various temperature conditions (−10, 0, 10, 25, and 50 °C) to explore the feasibility of using such environments.

1. Introduction

Fossil fuels are one of the most conventional forms of energy that we still use in our combustion engines. However, its impacts on the environment include global warming, air pollution, water pollution, *etc.* Replacing these non-renewable fossil fuels, we have clean, renewable energy sources such as wind, hydrothermal, biomass, *etc.* Nevertheless, storing these energies is still a significant challenge that we face today. Among the different electrochemical energy storage devices, Lithium-ion capacitors (LICs) are one of the promising energy storage devices. It is the recently developed device to bridge the gap between high-energy Lithium-ion batteries (LIBs) and high-power supercapacitors (SCs). LIC is the hybridization of battery-type electrodes (with the faradaic process) and capacitive-type electrodes (with the non-faradaic process), bringing a synergetic effect with high-energy and high-power density simultaneously in a single device. This can overcome the slow charging problem of LIBs and the lower energy density of SCs. However, their performance is still second-class for the applications in Electric vehicles (EVs) & Hybrid electric vehicles (HEVs) [1].

Commercialized LICs consist of an insertion-type, pre-lithiated graphitic carbon anode, and an activated carbon (AC) cathode. Since the battery-type electrode determines the overall energy density, power capability, and reaction rates of the LICs, hence, the researchers are mainly focussing on different anode materials used in LICs [2–7]. Among the different kinds of battery-type materials, insertion types (Graphite, $Li_4Ti_5O_{12}$, *etc.*) [8,9] are well explored, but they lack energy density for high-end applications because of the limited specific capacity and reversibility. Researchers are now converged into conversion/alloying type (mainly transition metal oxides) electrode materials because of their high theoretical capacity originating from the multi-electron reactions [10–13]. Among the transition metal oxides, CuO is one of the promising electrode materials with high theoretical capacity (~674 mAh g^{-1}), conductivity, chemical stability, abundance, and low cost. One of the major drawbacks of using such alloy/conversion-based

* Corresponding authors.
E-mail addresses: leeys@chonnam.ac.kr (Y.-S. Lee), aravind_van@yahoo.com (V. Aravindan).

https://doi.org/10.1016/j.susmat.2023.e00603
Received 21 September 2022; Received in revised form 1 March 2023; Accepted 16 March 2023
Available online 22 March 2023

anode is the volume variation (thereby cycling instability) and kinetic limitations due to different mechanisms in the two electrodes of LICs. So, various attempts exist to use different composites as anodes where intercalation and conversion/alloying co-occur [14–16].

Our work utilizes conversion-type recovered CuO and intercalation-type recovered graphite (RG) composite as anode for LICs. Using RG:CuO composite as an anode can bring down the kinetic limitations and enhance the overall performance of LICs. The CuO and Graphite were regenerated and recovered from the anodic current collector (Copper foil) and the anodic active material of the spent LIB. We have already optimized the calcination temperature and dwelling time to synthesize CuO, and the best electrochemical performance was obtained at 500 °C and 2 h of dwelling time. The electrochemical performance of Li/CuO half-cells was also compared using two different binders: carboxymethyl cellulose (CMC) and polyvinylidene fluoride (PVdF) [17]. The water-soluble CMC binder exhibited far better electrochemical performance than the PVdF binder. The unsaturated $> C = CF-$ bonds, low flexibility, swelling at raised temperature, harmful solvents like *N*-methyl–2-pyrrolidinone (NMP), risk of thermal runaway of cells, *etc.* are some of the drawbacks of PVdF binder, which limits its performance [18–20]. Hence, we used this aqueous binder for our entire studies, and using this binder impacted a considerable change in the specific capacity, cyclic performance, *etc.* [17].

In this work, we completely recovered the anode part (active material & current collector) of spent LIBs and re-used it as an anodic active material for LIC. Also, the choice of binder is also studied in half-cell assembly, which strongly encourages us to use eco-friendly water as a solvent rather than hazardous NMP. Poor solid-electrolyte interphase (SEI) formation is one of the prime issues for the conversion and alloy-type anodes, which is effectively tackled by introducing the concept of the insertion-conversion process by employing graphite anode *via* mechanical milling. This eventually results in enhanced cyclability in both half- and full-cell assemblies. Finally, the LIC is fabricated with all the compositions, and its feasibility under various environmental conditions is explored and discussed in the forthcoming sections.

2. Experimental section

Recovery of Copper foil and Graphite: The spent mobile phone and laptop batteries were collected from the local market. It is then immersed in NaCl solution overnight for the complete discharge. The completely discharged batteries were picked out for dismantling by checking the open-circuit potential. These batteries were washed in distilled water and kept in a hot air oven at 65 °C for 4 h. The dried batteries were taken out and manually disassembled in the fume hood using cutters and pliers.

The LIBs consist of a graphite anode, numerous metal oxides or phosphates cathode, and a polyolefin separator. The graphite is coated over copper foil current collector and cathodic active material over aluminum foil. The anode, cathode & separator are taken out from the dismantled battery and are separated. The cathode & separator were separately stored in different containers for future recovery and re-use. The anode is immersed in distilled water and sonicated to remove the graphite from the copper foil. The copper foil is then submerged in dimethylformamide (DMF, Sigma Aldrich, anhydrous, 99.8%) to completely remove graphite and binders stuck on the copper foil. The clean copper foil thus obtained is washed using distilled water, dried in the oven, and then stored in the dry box [17,23].

The graphite was recovered using a different method. First, the anode from the dismantled battery is taken out, and the graphite stick to copper foil is scratched out. It is then immersed in DMF with constant stirring under heating for 24 h at 90 °C to remove the binder (Polyvinylidene fluoride, PVdF) used in coating graphite over Cu foil. The graphite thus obtained was filtered using suction filtration and was dried in the box furnace (Carbolite, UK) at 150 °C for 12 h. Hence, the obtained Graphite was used in the composite as an anode for LICs [24].

Synthesis of CuO: For the synthesis of CuO, the small pieces of recovered copper foil were dissolved in the nitric acid to get the copper nitrate ($Cu(NO_3)_2$) solution. It is made up to 250 ml using double-distilled water, and then the previously prepared 1 M sodium hydroxide (NaOH) was added dropwise to it with continuous stirring. Thus, the copper hydroxide ($Cu(OH)_2$ was precipitated. NaOH was then added to it until the solution became slightly basic to ensure the complete precipitation of the $(Cu(OH)_2$. The precipitate is collected and washed multiple times with double-distilled water until the pH drops to 7. The neutral solution is then centrifuged at 4000 rpm for 5 min to separate the precipitate. The $(Cu(OH)_2$ precipitate was dried overnight at 65 °C. It is then powdered using the mortar & pestle and calcined at 500 °C for 2 h to obtain nanosized CuO [17,25].

Materials characterization: Powder X-ray diffraction (XRD) was performed using Rigaku D/teX Ultra 250 diffractometer (40 kV, 200 mA, $\lambda = 1.5406$ Å) with Cu Kα radiation for the phase identification of r-CuO, RG, and different RG:CuO composites from 10° to 80° at a scan rate of 0.5° min^{-1}. Raman spectroscopy analysis was done for all the composites using Lab Ram HR800 UV Raman microscope (Horiba Jobin-Yvon, France) with a 515 nm Diode laser as an excitation light source. Morphology of different composites was analyzed using a field-emission scanning electron microscope (FE-SEM S-4700, Hitachi, Japan) and internal structure using a High-resolution transmission electron microscope (HR-TEM, TECNAI, Philips, the Netherlands, 200 keV). X-ray photoelectron spectroscopy (XPS, Multilab 2000, UK; monochromatic Al Kα radiation $h\nu = 1486.6$ eV) was performed for the surface electronic state identification and the elemental composition analysis was carried out using High angle annular dark-field imaging (HAADF) detector and Energy-dispersive X-ray spectroscopy (EDS).

Electrochemical analysis: Firstly, the different RG(100):CuO(0), RG(75):CuO(25), RG(50):CuO(50), RG(25):CuO(75), and RG(0):CuO (100) were prepared using planetary ball-milling for 30 min with composite: planetary balls ratio 1:20. The electrodes of different composites were fabricated separately using the conventional slurry coating method. Initially, For the slurry preparation, 80 wt% active material (different composites), 10 wt% conductive carbons (acetylene black), and 10% binder (Carboxymethyl cellulose, CMC) were mixed using the water solvent and kept for stirring for 8 h to get a homogenous slurry. The slurry is coated on copper foil using the doctor blade apparatus (MSK-AFA-III Automatic Thick Film Coater (MTI Corporation). For drying, the uniformly coated active material was kept overnight in a hot air oven at 65 °C. The 14 mm electrode cutter was used to punch out the electrodes used as the anode. At the same time, the cathode is commercial activated carbon (YP 80F Kuraray, Japan; Surface area: 2100 m^2 g^{-1}, Pore volume: 0.97 ml g^{-1}) that was hand-made using mortar and pestle with AC, acetylene black (conductive carbon) and binder (teflonized acetylene black – TAB-2) mixed in the ratio 8–1-1 ratio using ethanol solvent. The thin layer of the electrode thus obtained was then pressed on a stainless-steel current collector (Goodfellow, UK) and dried at 75 °C in the vacuum oven for 4 h.

The coated RG:CuO and hand-made AC electrodes were subjected to both half-cell and full-cell studies. The CR2016 type coin-cells were fabricated inside an Argon-filled glove box (MBraun, Germany) with an O_2 level < 0.1 ppm and H_2O level < 0.1 ppm. 1 M $LiPF_6$ dissolved in ethylene carbonate (EC), and dimethyl carbonate (DMC) in a 1:1 ratio (Tomiyama, Japan) was the electrolyte used, and Whatman paper (1825–047, GF/F) separator physically separated the anode and cathode from touching each other. For RG:CuO composite and AC electrodes, Lithium metal was the counter/reference electrode in half-cell assembly. The AC/RG:CuO composites hybrid capacitor was fabricated such that the half cells (Li/RG:CuO & Li/AC) were initially pre-lithiated. The half-cells were cycled for two complete charge-discharge cycles, and then the cell was dismantled in discharge state (LiC_6, & $Cu^0 + Li_2O$) and paired with an AC electrode (mass balanced) to get AC/RG:CuO hybrid capacitor. The galvanostatic charge-discharge (GCD), Electrochemical impedance spectroscopy (EIS), and Cyclic voltammetry (CV) studies

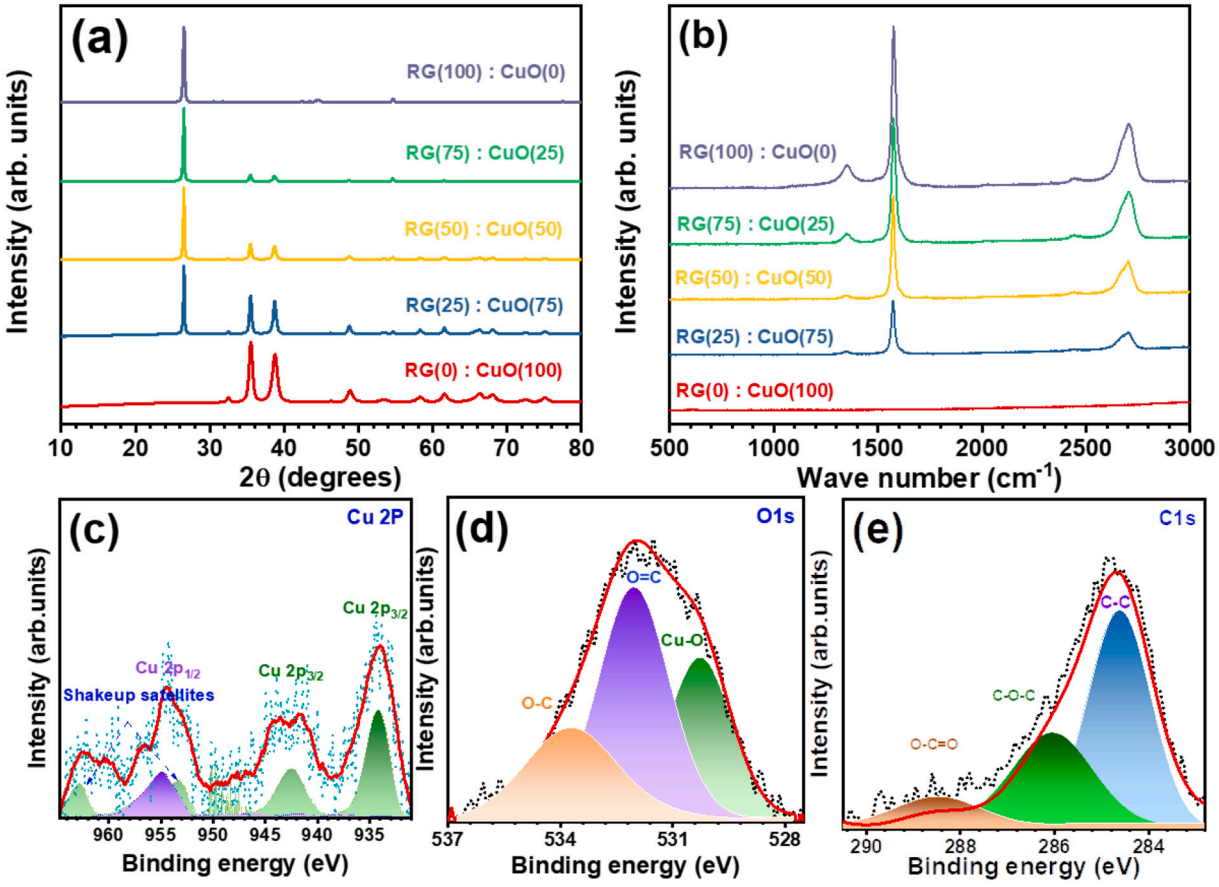

Fig. 1. Physical characterization: (a) XRD patterns, (b) Raman spectra, (c, d & e) deconvoluted XPS spectra of RG(50):CuO(50) composite: high-resolution spectrum of (c) Cu 2p, (d) O 1 s, and (e) C 1 s.

were performed using the Biologic BCS 805 (France) battery tester. The temperature dependence of LIC was also analyzed by performing electrochemical studies at different temperatures using an environmental chamber (Espec, Japan).

3. Result and discussion

X-ray diffraction (XRD) studies were used to analyze the crystallographic structure, phase purity, and physical properties of RG, CuO, and ball-milled RG:CuO composites (Fig. 1a). The composites with RG:CuO ratios of 100:0, 75:25, 50:50, 25:75 & 0:100 were formulated by using the planetary ball miller for 30 min. After the milling process, no heat treatment was employed for the composites, and they were directly employed as a battery-type electrodes. The XRD peaks with a hexagonal crystal structure (a = b = 2.464 Å, c = 6.736 Å; α = 90°, β = 90°, γ =120°) having 194: P63/mmc space group indexed with standard data (DB Card Number: 00–012-0212). The CuO exhibits a monoclinic crystalline structure (a = 4.69 Å, b = 3.42 Å, c = 5.131 Å; α = γ =90°, β = 99.54°) with 15: C12/c1 space group (DB Card Number: 01–089-5898, JCPDS card number: 48–1548). The other three composites (RG:CuO) have the XRD reflections corresponding to both RG and CuO, and there is no new peak appears, which clearly indicates the purity of the phase. An increase in the intensity of the CuO phase is evident in the composite with an increase in the concentration. The crystallite size of five different samples was calculated using Scherrer's eq. ($D = 0.9\lambda/\beta \cos\theta$). The crystalline sizes for RG(100):CuO(0), RG(75):CuO(25), RG(50):CuO (50), RG(25):CuO(75), and RG(0):CuO(100) composites are calculated to be 22.98, 25.17, 21.27, 19.06, and 9.44 nm, respectively.

The Raman spectra of all the composites are given in Fig. 1(b). All the samples, except bare CuO, show characteristic peaks corresponding to D, G, and 2D bands at ~1350, ~1600, and ~ 2700 cm^{-1} of carbonaceous materials. The increase in peak intensity is also observed with an increase in the graphitic percentage. The D band, also called the defect or dispersive band, corresponds to the structural defect caused by the n-number of cycles in the LIB assembly. The G band is attributed to the in-plane stretching of sp^2 carbon atoms. The intensity ratio between the D band & G band estimates the degree of graphitization. The calculated I_D/I_G ratios are 0.25, 0.05, 0.09, and 0.07 for RG(100):CuO(0), RG(75):CuO (25), RG(50):CuO(50), and RG(25):CuO(75) composites, respectively. The lower I_D/I_G ratio values for the composites are mainly associated with the removal of the weakly bonded graphene layers in the RG, in which the presence of CuO particles aids in attaining such a more ordered graphitic structure since the planetary milling was not performed for the case of RG(100):CuO(0). Hence, the weakly bonded graphene layers attached, resulting in slightly increased disorders. We have done the surface chemical compositions very selectively since there is no different routes or approaches were employed for the preparation of the composites except the concentration. The surface elements of the RG (50):CuO(50) sample were detected using an XPS survey and consist of the peak corresponding to Cu (copper), O (oxygen), and C (carbon). The XPS spectrum of Cu 2P (Fig. 1c) has two prominent deconvoluted peaks positioned at ~934.15 and ~ 954.8 eV, corresponding to Cu $2p_{3/2}$ and Cu $2p_{1/2}$, respectively, and two satellite peaks positioned at ~962.75 and ~ 953.25 eV. The satellite peaks originated during the shake-up process, occurring when the electrons excite to higher energy levels. These satellite peaks indicate the 2+ oxidation of the Cu state in CuO. The deconvoluted O 1s spectra (Fig. 1d) have three peaks observed at ~533.7, ~532.05, and ~ 530.3 eV. The peaks located at ~533.7 and ~ 532.05 eV correspond to the O in O═C and O—C, respectively, formed by the graphitic oxidation when exposed to air. Furthermore, the peak at

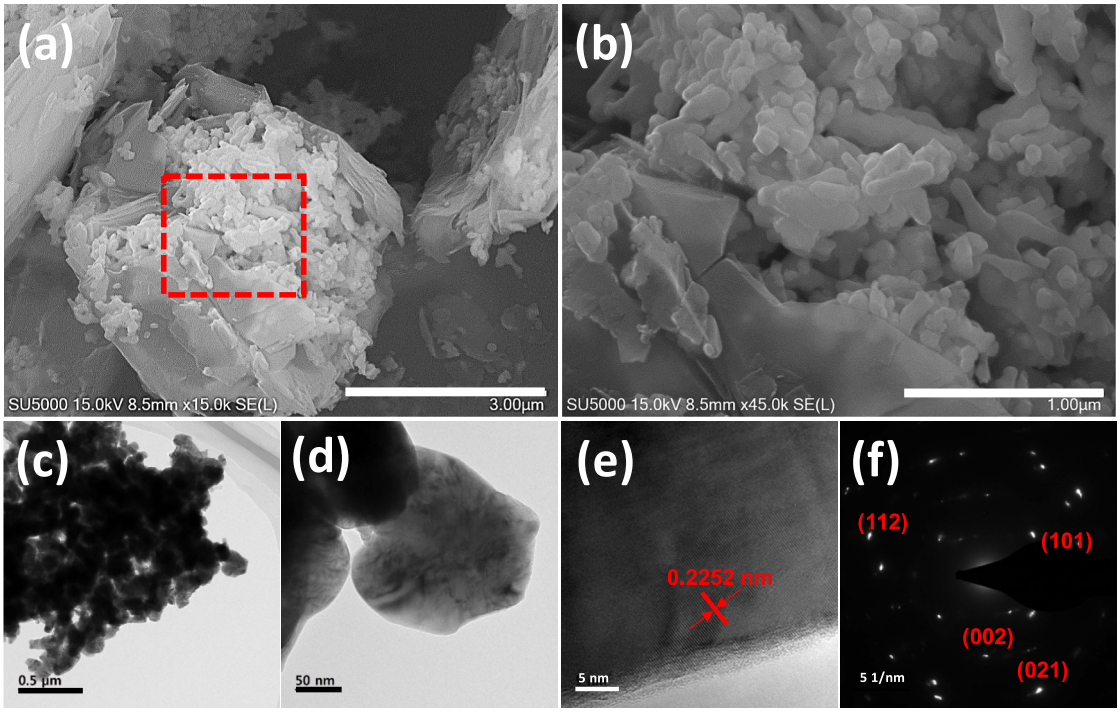

Fig. 2. (a, b) FE-SEM of RG(50):CuO(50) with two different magnifications, (c, d) TEM of RG(50):CuO(50) with different magnifications, (e) HR-TEM, and (f) SAED pattern.

~530.3 eV indicates the O in CuO. We could see the appearance of three deconvoluted peaks of C 1s (Fig. 1e) at ~288.5, ~286.05, and ~ 384.6 eV, corresponding to the C in O-C=O, C-O-C, and C—C, respectively.

The surface morphological features of all the five different RG:CuO composites are given in fig. S1 (a-j). The bare RG (fig. S1 (a, b)) shows flaky morphology, whereas the bare CuO (fig. S1 (i, j)) has agglomerated particulate morphology. In the case of composites, we could see combined features of CuO and RG morphologies. Fig. 2 (a, b) shows an equal mixture of flaky and particulate morphology for RG(50):CuO(50) composite. Also, we can see that with the increase in CuO concentration, there is an increase in agglomeration of the CuO particulates attached to the graphitic flakes. The size, morphology, and internal structure of the RG(50):CuO(50) composite were further investigated using HR-TEM analysis. Fig. 2(c-e) shows the TEM picture at different magnifications and confirms the adsorption of r-CuO nanospheres on the graphitic flakes (Additional TEM images are given in the supplementary information; Fig. S2). The lattice fringes *d* spacing was calculated and found to be 1.126 Å. The crystalline nature of RG(50):CuO(50) was confirmed by the series of brightly spotted concentric diffraction rings in the selected area electron diffraction (SAED) pattern (fig. 2(f)). The observed SAED spots clearly indicate the single crystalline nature of the CuO crystals subjected to the HR-TEM analysis. Further, the observed SAED spots were assigned corresponding lattice planes.

4. Electrochemical studies

A series of cyclic voltammetric (CV) measurements were carried out for all the compositions to evaluate their electrochemical performance (Fig. 3(a)). Fig. S3(a-e) displays the first 6 cycles of CV traces of RG (100):CuO(0), RG(75):CuO(25), RG(50):CuO(50), RG(25):CuO(75), and RG(0):CuO(100) composites, measured at a scan rate of 0.2 mV s^{-1}. All the composites were formulated with the CMC binder. The CV traces show a prominent cathodic peak in the CV of bare RG at 0.11 V *vs.* Li, corresponding to characteristic LiC_6 formation by the staging process during the lithiation ($6C + Li \rightarrow LiC_6$). The noticeable anodic peak at 0.26 V *vs.* Li indicates the Li^+ ions extraction from the graphite intercalation compound, LiC_6 ($LiC_6 \rightarrow 6C + Li$). Apparently, there is no difference between the first and subsequent cycles, which indicates the structural integrity of the well-known insertion host, even after *n* number of repeated charge-discharge cycles. The most prominent reduction peaks at 1.1, 1.16, and 1.18 V *vs.* Li of three composites, RG (75):CuO(25), RG(50):CuO(50), and RG(25):CuO(75), indicates the structural destruction and associated electrolyte decomposition. This leads to the formation of the irreversible SEI layer formation. However, the electronic conductivity of the bare CuO is inferior compared to the CuO:RG composite. Hence, the on-set reduction potential of the CuO is marginally shifted toward the lower potential region *vs.* metallic Li. This peak's intensity is dramatically reduced from the second cycle onwards with a shift toward the lower potential region. Moreover, for all three composites, noticeable reduction (during discharge) and oxidation peaks (during charge) are present around 0.8, 0.11, 1.19, & 2.2 V and 0.26, 1.4, 2.5 & 2.7 V *vs.* Li, respectively, from the second cycle onwards. The reduction peak around 2.2 V *vs.* Li attributes to the partial reduction of CuO to $Cu^{II}_{1-x}Cu^{I}_{x}O_{1-x/2}$ solid solution phase ($0 \leq x \leq 0.4$) and the other two reduction peaks at 1.18 & 0.7 V *vs.* Li corresponds to the Cu_2O and Cu^0 formation, respectively ($CuO + Li \rightarrow Cu^0 + Li_2O$) [17,21]. The oxidation peaks observed at 2.5 and 2.7 V *vs.* Li indicate the re-formation of $Cu^{II}_{1-x}Cu^{I}_{x}O_{1-x/2}$ and subsequently CuO phase ($Li_2O + Cu^0 \rightarrow CuO$). As observed, the anodic peak at 0.26 V *vs.* Li corresponds to the Li^+ ion extraction from graphite. We could see that while moving from the CV curve of RG(75):CuO(25) to RG(25):CuO(75), the intensity of CuO peaks increases, and the graphitic peak intensity reduces, which is directly related to the material composition of the composite. About the RG(0): CuO(100) composite is concerned, the redox reactions of the conversion type CuO remain the same and occur in the same potential, except for the Li-intercalation process due to the presence of RG.

The galvanostatic charge-discharge (GCD) analysis was performed for all the composites, in which RG(100):CuO(0) composite, the potential window is limited to 0.005 to 2.5 V *vs.* Li, and in other compositions, the testing region is extended as 0.005 to 3 V *vs.* Li at a current rate of 0.1 A g^{-1} (fig. S4 (a-e)). At first, the electrochemical studies of CuO were carried out using the conventional PVdF binder. However, the

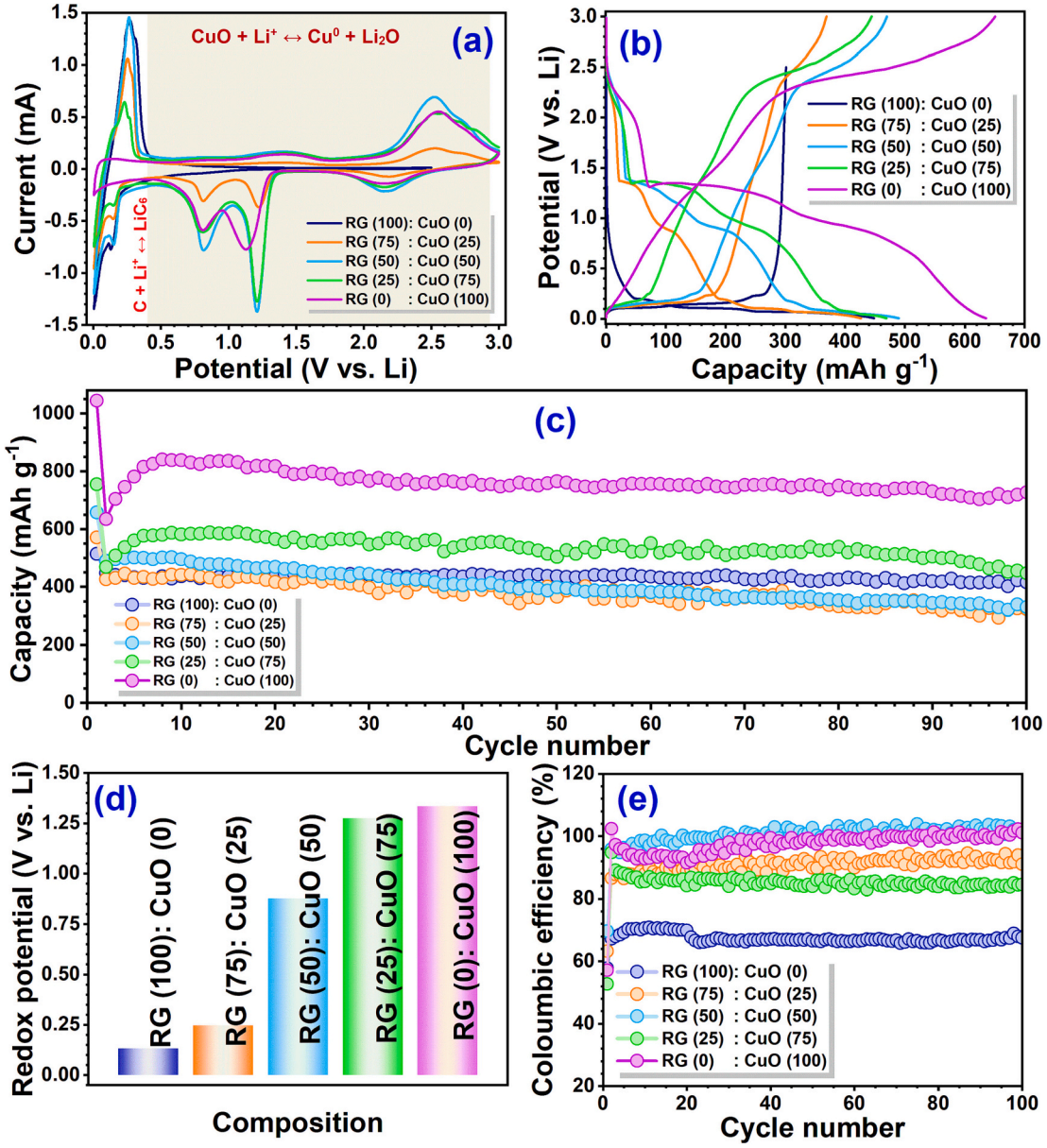

Fig. 3. (a) Comparison of CV profiles of all the composites (second cycle), (b) charge-discharge profile comparison (second cycle) of all the composites, (c) cycling performance of different composites, (d) comparison of the redox potential of the different composites, and (e) comparison of the coulombic efficiencies of different RG:CuO composites.

cyclic stability is inferior due to the presence of unsaturated > C = *CF*– bonds and poor compatibility. As a result, the specific capacity is drastically reduced to 110 mAh g^{-1} within 40 cycles. Hence, we attempted the possibility of using a water-soluble, environmentally friendly CMC binder. A remarkable improvement in the electrochemical performance is noted, which clearly suggests that a passive component, the binder, also plays a vital role in the electrochemical performance of the active material. In the case of the CMC binder, there is a robust ester-like linkage between the active material and polymer molecules due to the carboxylic group. It brings out strong adhesion and thereby provides better cyclic performance. However, such bonds are absent in the case of the PVdF binder. They are bound by a fragile hydrogen bond between the active material and the fluorine atom of the binder [17]. Fig. S5 shows the GCD comparison of conversion type CuO with two different binders. The CuO showed a stable cyclic performance for more than 120 cycles with >99% coulombic efficiency. It has an initial discharge capacity and charge capacity of ~1046 and ~ 597 mAh g^{-1}, respectively, with the CMC binder. The initial irreversible loss in capacity is due to the formation SEI layer. Moreover, with the increase in the cycle number, the capacity increases and then stabilizes, which could be due to further activation of the electrochemical sites [17].

The electrochemical performance of RG in a half-cell configuration is also compared using the two different binders (fig. S6). The GCD comparison (fig. S6 (b&d)) depicts that the graphite half-cell with CMC binder exhibits better performance in terms of specific capacity, but its coulombic efficiency is found to be very poor (less than 70%). On the other hand, the RG half-cell with PVdF binder has a constant specific capacity of ~300 mAh g^{-1} with >99% coulombic efficiency (fig. S6 (e)). However, in the case of composites, the presence of CuO content dramatically improves the coloumbic efficiency irrespective of the concentration the in the presence of a CMC binder. Therefore, we have conducted all the electrochemical studies with a CMC binder, although the RG exhibits inferior coloumbic efficiency. The half-cell studies of different composites were performed and are shown in Fig. 3. The initial

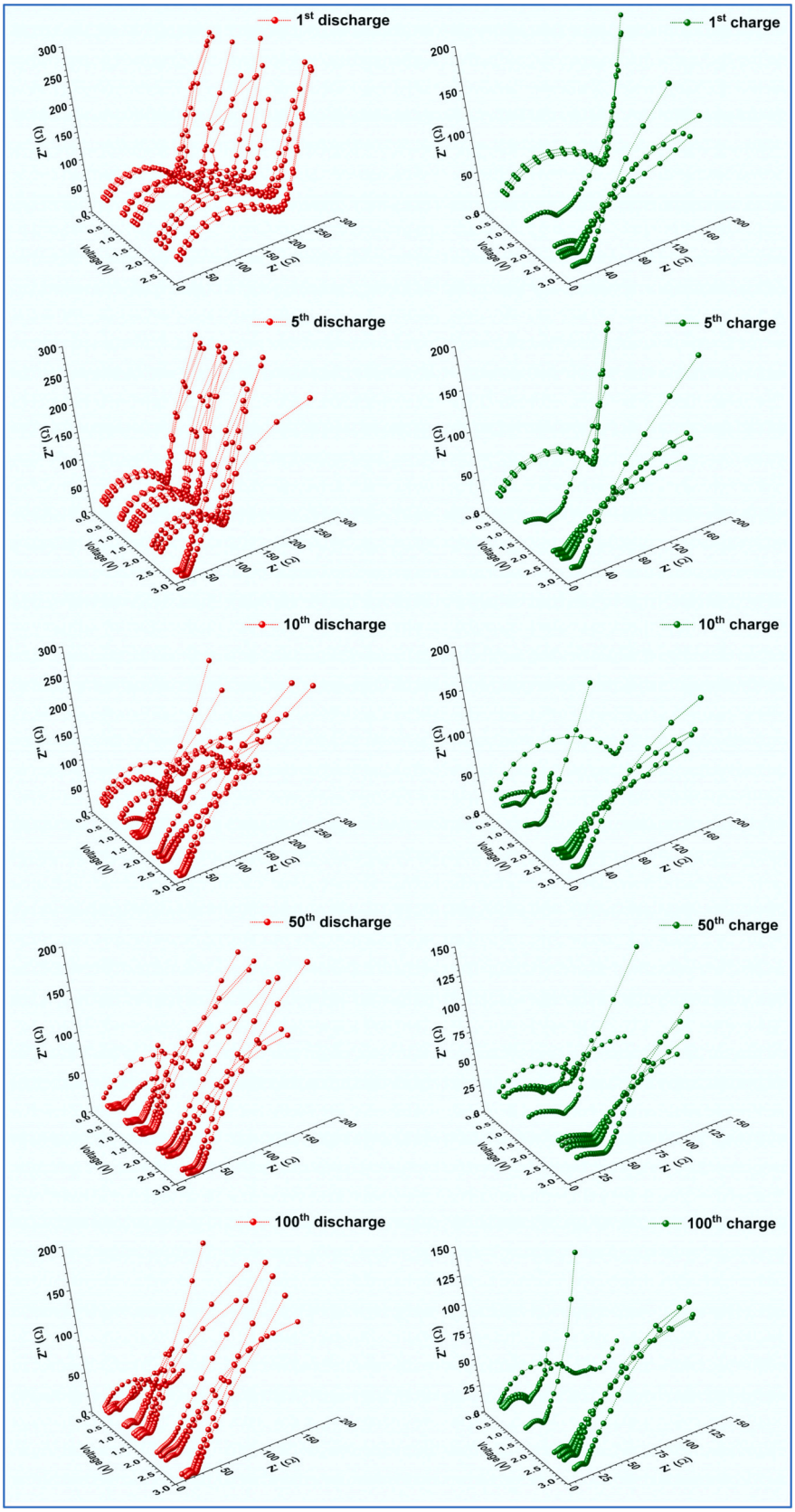

Fig. 4. *In-situ*-electrochemical impedance spectroscopy (*in-situ*-EIS) profile of RG(50):CuO(50) half-cell. Impedance profile of 1st, 5th, 10th, 50th, and 100th charge-discharge at different potentials.

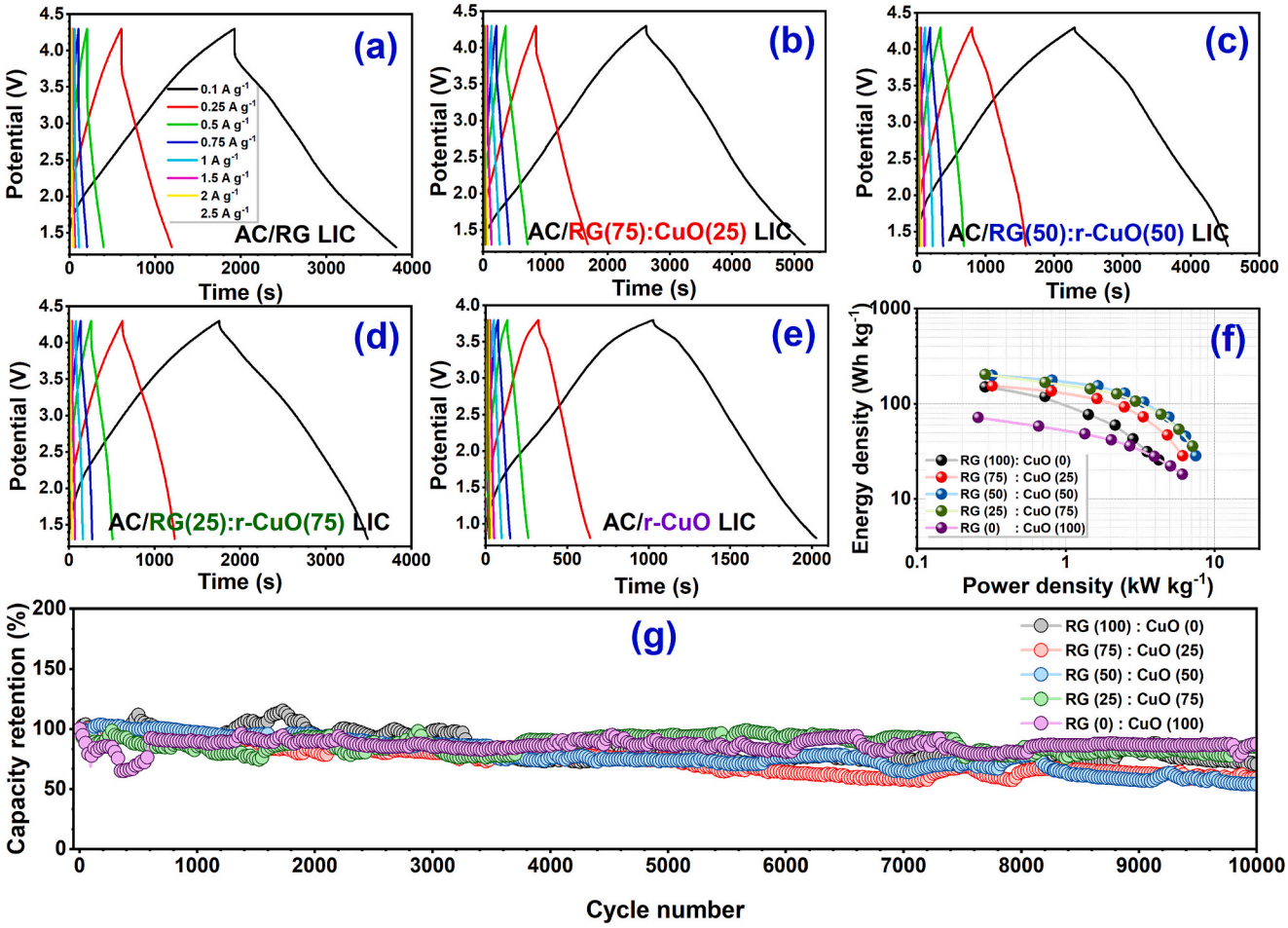

Fig. 5. Electrochemical performance of fabricated AC/RG:CuO composites based LICs: (a-e) Galvanostatic charge-discharge at different current rates, (a) AC/RG (100):CuO(0), (b) AC/RG(75):CuO(25), (c) AC/RG(50):CuO(50), (d) AC/RG(25):CuO(75), (e) AC/RG(0):CuO(100), (f) Ragone plot of different LICs, and (g) cyclic stability of different LICs.

discharge capacity of RG(100):CuO(0), RG(75):CuO(25), RG(50):CuO (50), RG(25):CuO(75), and RG(0):CuO(100) are ~515, ~572, ~643, ~756, and ~ 1046 mAh g^{-1}, respectively, with coulombic efficiencies ~58, ~63, ~59, ~53 and ~ 57%. The GCD profile is given in Fig. 3(b), which shows a comparison between different composites and matches well with the CV plots obtained. The CV profile shows the evolution of the conversion reaction from the intercalation mechanism as we move from fig. S3 (a) to (e). The rate capabilities of all the composites from 0.05 to 1.5 A g^{-1} for every six cycles were analyzed and are given in fig. S7. The average discharge capacity of RG(100):CuO(0), RG(75):CuO (25), RG(50):CuO(50), RG(25):CuO(75), and RG(0):CuO(100) composites at a current density of 0.05 A g^{-1} is found to be ~344, ~408, ~563, ~525, and ~ 838 mAh g^{-1}, respectively. The RG(50):CuO(50) composite exhibits better average discharge capacity than the other composites except for the RG(0):CuO(100) composite. But while considering the coloumbic efficiency, we could observe that the former has an average coloumbic efficiency of ~97%, whereas the latter has retained only ~82.9%. Even when the current rate is increased to 1.5 A $g^{-1,}$ the average capacity of RG(50):CuO(50) is maintained at 225 mAh g^{-1}. Moreover, it retained a specific capacity of 552 mAh g^{-1} when the current rate is switched to 0.05 A g^{-1}. The cyclic stability of the composites is given in Fig. 3(c), where we can see that all the composites exhibit better stability for more than 100 cycles. An increase in the redox potential is also evident as we move from bare RG to bare CuO (Fig. 3 (d)). The redox potential of the composite is calculated at the intersection potential of the charge-discharge curves. Even the bare CuO exhibits better capacity, stability, and coloumbic efficiency than other composites, but its higher redox potential is one of the prime issues which eventually dilutes the net working potential of the cell. Therefore, by considering all the parameters like capacity, stability, redox potential, and coloumbic efficiency, the RG(50):CuO(50) composites is found to be synergistically favourable to achieving high-performance LICs.

The *in-situ*-electrochemical impedance spectroscopy (*in-situ*-EIS) study was performed on RG(50):CuO(50) to analyze the compatibility and SEI formation for stable performance of the CuO and RG composite and is given in Fig. 4. In the first discharge, we could see a high charge transfer resistance (R_{CT}) >200 Ω, mainly due to the initial irreversibility originating from the electrolyte decomposition caused by the SEI layer formation. As the cycling progresses, we can see that the R_{CT} decreases, and after the 10th cycle, we can see almost constant values. From this, we can say that it took 10 cycles of charge-discharge to form a stable and robust SEI layer after some structural rearrangements. We can also see that the R_{CT} of the 100th cycle is comparable with that of the 10th cycle, which concludes that the SEI layer formed is very robust. In addition, the *in-situ*-EIS of RG(0):CuO(100) is also recorded, and the representative traces were given for 1st, 2nd, 5th, 10th and 18th cycles (fig. S8). While comparing with RG(50):CuO(50), the RG(0):CuO(100) has high R_{CT} for the initial cycles, and it further increases as the cycle progresses. Whereas for the former, we could clearly observe a drop in the R_{CT}, and it becomes stable for 100 cycles, indicating the dominance of the RG: CuO composite over the bare CuO. This robust SEI layer is one of the prime reasons for the stable electrochemical activity of the RG:CuO composite in half-cell assembly and is also anticipated to render the same performance in full-cell configuration.

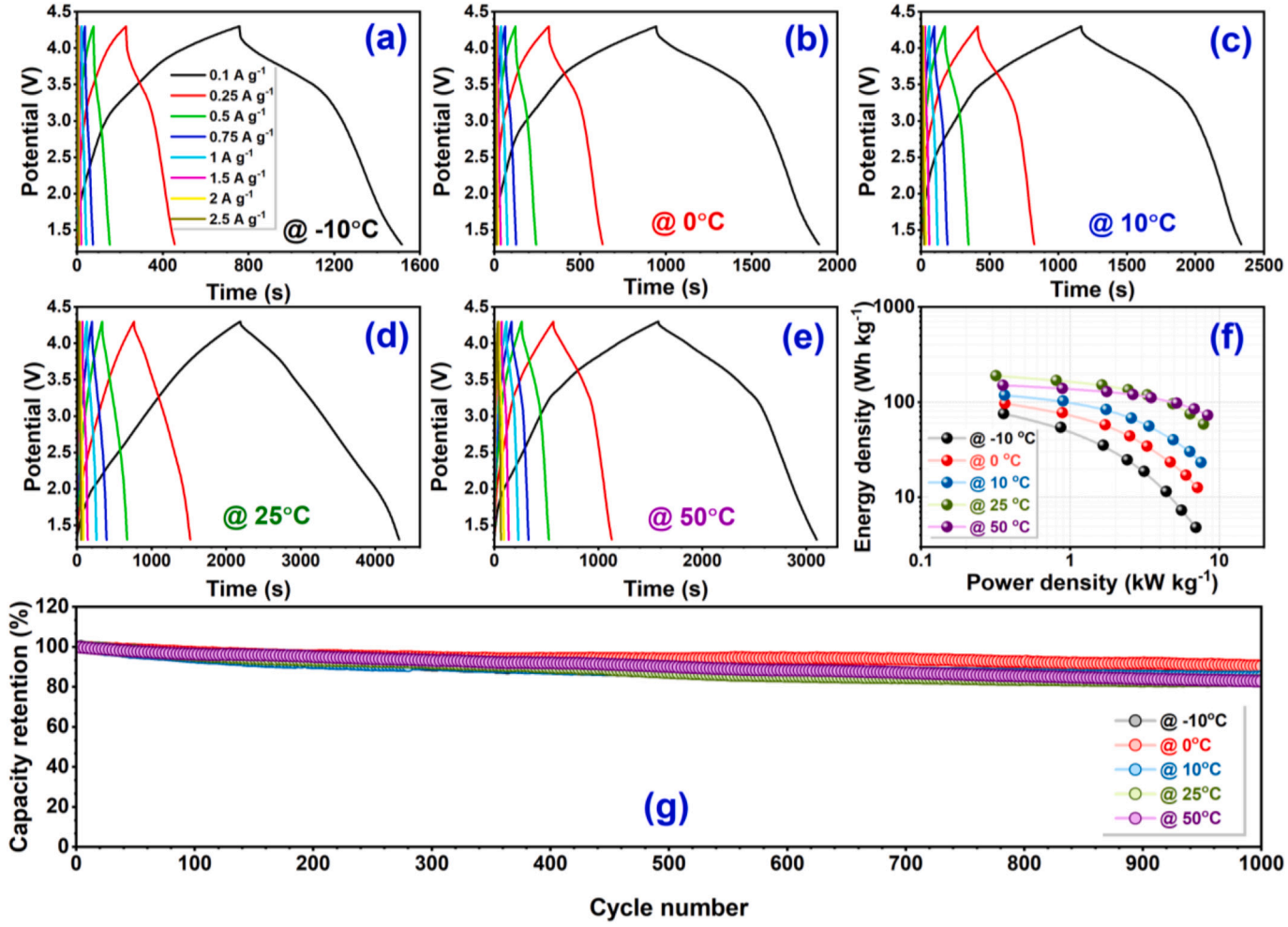

Fig. 6. Electrochemical performance of AC/RG(50):CuO(50)-based LIC: (a-e) galvanostatic charge-discharge curves at different temperatures, (f) Ragone plot showing energy density and power density values, and (g) long-term cyclic performance at a current density of 1.5 A g^{-1} at different temperatures.

The Li/AC half-cell performance was also evaluated from 1.5 to 4.5 V *vs.* Li potential range at the current rate of 0.2 A g^{-1}. It showed an initial discharge capacity of 135 mAh g^{-1} and retained the discharge capacity of 110 mAh g^{-1} after 500 cycles. The linear GCD (fig. S9) of the Li/AC half-cell depicts the pure non-faradaic adsorption/desorption of Li^+ & PF_6^- ions during the charge-discharge process. The LIC is fabricated to hybridize the composite anodes with AC cathodes. Here, the two electrodes have different energy storage mechanisms. The battery-type composite electrodes exhibit a faradaic energy storage mechanism by redox reactions, *i.e.*, conversion and intercalation, whereas the AC cathode shows non-faradaic adsorption/ desorption type energy storage. Hence, a kinetic imbalance exists between the two electrodes during the charge-discharge process. In order to mitigate this issue, mass balancing is necessary during the assembly of cells. The equation of mass balancing is as follows:

$$M_1C_1 = M_2C_2$$

Where M_1 is the mass of RG:CuO composites, M_2 is the mass of AC, C_1 is the specific capacity of RG:CuO composites and C_2 is the specific capacity of AC.

For the fabrication of the LIC, the different r-CuO composite half-cells were pre-lithiated, then dismantled, and paired with the AC electrode. Initially, the Li/RG:CuO composite half-cells were fabricated. It is then subjected to an initial discharge followed by two complete charge-discharge cycles. These half-cells are dismantled after the third discharge to ensure the lithiated product (LiC_6, $CuO^0 + Li_2O$) and paired with the mass-balanced AC electrode. The electrochemical performance of five different RG:CuO composites in full-cell assembly with AC at room temperature are shown in Fig. 5. Among the different AC/RG:CuO composite-based hybrid capacitors, the RG(50):CuO(50) showed better electrochemical performance. The Ragone plot in Fig. 5(f) compared the energy density & power density of different composites, showing their performance at different current rates. The LIC, with anode/cathode mass loading 2.64 and 10.02 mg, delivers a maximum energy density of 198.7 Wh kg^{-1} and a power density of ~7.5 kW kg^{-1} at room temperature. The observed energy density is in order of magnitude higher than bare CuO (71.54 Wh kg^{-1}), which is mainly due to the higher redox potential of the conversion reaction. On the other, the RG(50):CuO(50)-based LIC outperformed the bare RG (150.62 Wh kg^{-1}) as well. Therefore, the synergistic effect of both conversion and intercalation reaction eventually results in realizing the high energy density. The observed values are comparable with reported conversion/alloy and insertion-type electrode-based LICs summarized in our reviews [22]. Further studies are in progress to improve the energy density of such LICs, especially at higher power rates. Long-term cyclic stability is one of the prime aspects of the charge-storage system, irrespective of the active materials and assemblies. In this line, long-term cyclability is conducted at a current density of 1.5 A g^{-1} and given in Fig. 5g. The LICs, AC/RG (100):CuO(0), AC/RG(75):CuO(25), AC/RG(50):CuO(50), AC/RG(25):CuO(75), and AC/RG(0):CuO(100) retained the 80, 74, 74, 86 and 94% initial capacity after 5000 cycles. Although the AC/RG(0):CuO(100) configuration exhibited better cyclability, but the energy density is

lower than the other composite-based configurations.

Based on the high energy, cyclability, and performance, we have further studied the possibility of using AC/RG(50):CuO(50)-based LIC for various environmental conditions. Therefore, the AC/RG(50):CuO (50) cell is subjected to various temperature conditions like (−10, 0, 10, 25 & 50 °C) for 1000 cycles, as given in Fig. 6. When comparing the electrochemical performance under different temperature conditions, the better energy density is noted at 50 °C, especially at higher current rates. Achieving high energy at higher rates is one prerequisite for the practical applications of LICs. An increase in the ionic conductivity at high temperatures is the prime reason for the excellent performance [9]. However, inferior performance is noted at low temperatures (−10, 0 & 10 °C), which is mainly due to the freezing of the electrolyte. Apparently, there is not much deviation from the cycling profile noted irrespective of the testing environments. This clearly shows the synergistic effect of the conversion and insertion-type electrodes. Further studies are in progress to improve the energy density of the LICs, especially at higher current rates, without compromising the cycling profiles.

5. Conclusion

Our study used simple methods to recover the Cu-foil current collector and graphite from spent LIBs and its utilization as anode for LICs. We also replaced the conventional PVdF binder with a water-soluble, environmentally friendly CMC binder to have better Li/RG:CuO performance and a green chemistry approach. The different RG:CuO composites were made from ball milling the samples, and their performance was evaluated. Among the RG:CuO composites, the RG(50):CuO(50) composite exhibited better electrochemical performance in full-cell assembly. The LIC delivered a maximum energy density of ~198.7 Wh kg^{-1} with excellent cyclic performance for more than 5000 cycles at a current density of 1.5 A g^{-1}. The rate performance and long-term cycling at different temperatures were performed to analyze its performance at different climatic conditions. The LIC exhibited better electrochemical performance at 50 °C compared to low temperatures (−10, 0, and 10 °C). From the excellent results, we can conclude that this combined intercalation-conversion type RG:CuO composites is one of the appropriate measures to increase the overall electrochemical performance of the hybrid charge storage system. On the other hand, the utilization of recovered current collector and graphite from spent LIBs as anode material in the second life at LIC provides a new pathway for the circular economy.

CRediT authorship contribution statement

Manohar Akshay: Conceptualization, Formal analysis, Investigation, Data curation, Writing – original draft. **Krishnan Subramanyan:** Formal analysis, Investigation, Data curation, Writing – original draft. **Yun-Sung Lee:** Writing – review & editing, Supervision, Project administration, Funding acquisition. **Vanchiappan Aravindan:** Conceptualization, Formal analysis, Investigation, Data curation, Writing – original draft, Writing – review & editing, Supervision, Project administration, Funding acquisition.

Declaration of Competing Interest

The authors declare that they have no known competing financial interests or personal relationships that could have appeared to influence the work reported in this paper.

Data availability

Data will be made available on request.

Acknowledgments

KS thanks the Department of Science & Technology (DST), Govt. of India, for the financial support through INSPIRE fellowship (IF180157). YSL acknowledges the financial support from the National Research Foundation of Korea (NRF) grant funded by the Korean government (Ministry of Science, ICT&Future Planning) (No. RS-2023-00208361). VA acknowledges financial support from the Science and Engineering Research Board, a statutory body of the DST, Govt. of India, through Start-up Research Grant (SRG/2020/000002) and Swarnajayanti Fellowship (SB/SJF/2020-21/12).

Appendix A. Supplementary data

Supplementary data to this article can be found online at https://doi.org/10.1016/j.susmat.2023.e00603.

References

[1] V. Aravindan, Y.S. Lee, Building next-generation Li-ion capacitors with high energy: an approach beyond intercalation, J. Phys. Chem. Lett. 9 (2018) 3946–3958.
[2] M. Akshay, S. Praneetha, Y.-S. Lee, V. Aravindan, Hierarchical SnO_2@PC@PANI composite via in-situ polymerization towards next-generation Li-ion capacitor by limiting alloying process with high energy, wide temperature performance, and cyclability, Electrochim. Acta 439 (2023), 141599.
[3] S. Natarajan, M. Akshay, V. Aravindan, $MnCO_3$ cuboids from spent LIBs: a new age displacement anode to build high-performance Li-ion capacitors, Small (2023) 2206226, n/a.
[4] L. Qin, et al., In-plane assembled single-crystalline T-Nb_2O_5 Nanorods derived from few-layered Nb_2CTx MXene Nanosheets for advanced Li-ion capacitors, Small Methods 4 (2020) 2000630.
[5] L. Qin, et al., Formation and operating mechanisms of single-crystalline perovskite $NaNbO_3$ nanocubes/few-layered Nb_2CT_xMXene hybrids towards Li-ion capacitors, J. Mater. Chem. A 9 (2021) 20405–20416.
[6] L. Qin, et al., Single-crystal Nano-subunits assembled accordion-shape WNb_2O_8 framework with high ionic/electronic conductivities towards Li-ion capacitors, Small 18 (2022) 2107987.
[7] J.-Y. Tan, et al., Hollow porous α-Fe_2O_3 nanoparticles as anode materials for high-performance lithium-ion capacitors, ACS Sustain. Chem. Eng. 9 (2021) 1180–1192.
[8] V. Aravindan, J. Gnanaraj, Y.S. Lee, S. Madhavi, Insertion-type electrodes for nonaqueous Li-ion capacitors, Chem. Rev. 114 (2014) 11619–11635.
[9] M.L. Divya, S. Natarajan, Y.-S. Lee, V. Aravindan, Achieving high-energy dual carbon Li-ion capacitors with unique low- and high-temperature performance from spent Li-ion batteries, J. Mater. Chem. A 8 (2020) 4950–4959.
[10] M.V. Reddy, G.V. Subba Rao, B.V.R. Chowdari, Metal oxides and oxysalts as anode materials for li ion batteries, Chem. Rev. 113 (2013) 5364–5457.
[11] F. Klein, R. Pinedo, B.B. Berkes, J. Janek, P. Adelhelm, Kinetics and degradation processes of CuO as conversion electrode for sodium-ion batteries: an electrochemical study combined with pressure monitoring and DEMS, J. Phys. Chem. C 121 (2017) 8679–8691.
[12] K. Cao, T. Jin, L. Yang, L. Jiao, Recent progress in conversion reaction metal oxide anodes for Li-ion batteries, Mater. Chem. Front. 1 (2017) 2213–2242.
[13] Y. Xu, et al., Porous CuO@C composite as high-performance anode materials for lithium-ion batteries, Dalton Trans. 49 (2020) 11597–11604.
[14] M.L. Divya, S. Praneetha, Y.-S. Lee, V. Aravindan, Next-generation Li-ion capacitor with high energy and high power by limiting alloying-intercalation process using SnO_2@graphite composite as battery type electrode, Compos. Part B Eng. 230 (2022), 109487.
[15] J. Zhang, et al., Preparation of advanced CuO nanowires/functionalized graphene composite anode material for lithium ion batteries, Materials (Basel, Switzerland) 10 (2017).
[16] S.-H. Lee, et al., Expanded graphite/copper oxide composite electrodes for cell kinetic balancing of lithium-ion capacitor, J. Alloys Compd. 829 (2020), 154566.
[17] M. Akshay, K. Subramanyan, M.L. Divya, Y.-S. Lee, V. Aravindan, Choice of binder on conversion type CuO nanoparticles toward building high energy Li-ion capacitors: an approach beyond intercalation, Adv. Mater. Technol. 7 (2023) 2200423.
[18] S.S. Zhang, K. Xu, T.R. Jow, Evaluation on a water-based binder for the graphite anode of Li-ion batteries, J. Power Sources 138 (2004) 226–231.
[19] R. Wang, et al., Effect of different binders on the electrochemical performance of metal oxide anode for lithium-ion batteries, Nanoscale Res. Lett. 12 (2017) 575.
[20] J. Ming, et al., The binder effect on an oxide-based anode in lithium and sodium-ion battery applications: the fastest way to ultrahigh performance, Chem. Commun. 50 (2014) 13307–13310.
[21] R. Sahay, et al., High aspect ratio electrospun CuO nanofibers as anode material for lithium-ion batteries with superior cycleability, J. Phys. Chem. C 116 (2012) 18087–18092.

[22] S. Natarajan, Y.-S. Lee, V. Aravindan, Biomass-derived carbon materials as prospective electrodes for high-energy lithium- and sodium-ion capacitors, Chem. Asian J. 14 (2019) 936–951.
[23] S. Natarajan, M. Akshay, V. Aravindan, Recycling/reuse of current collectors from spent lithium-ion batteries: benefits and issues, Adv. Sustain. Syst. 6 (2022) 2100432.
[24] S. Natarajan, D. Shanthana Lakshmi, H.C. Bajaj, D.N. Srivastava, Recovery and utilization of graphite and polymer materials from spent lithium-ion batteries for synthesizing polymer-graphite nanocomposite thin films, J. Environ. Chem. Eng. 3 (2015) 2538–2545.
[25] K. Subramanyan, M. Akshay, Y.-S. Lee, V. Aravindan, Fabrication of Na-ion full-cells using carbon-coated $Na_3V_2(PO_4)_2O_2F$ cathode with conversion type CuO nanoparticles from spent Li-ion batteries, Small Methods 6 (2023) 2200257.